Comparing Global Warming and Anthropogenic Heat Impacts on Extreme Precipitation in urbanized Pearl River Delta area based on Dynamical Downscaling

Kwun Yip Fung[1,5], Chi-Yung Tam[1,2], Tsz Cheung Lee[3] and Ziqian Wang[4,6]

[1] Earth System Science Programme, The Chinese University of Hong Kong, Hong Kong, China

[2]Shenzhen Research Institute, The Chinese University of Hong Kong, Shenzhen, China

[3] Hong Kong Observatory, Hong Kong, China

[4] School of Atmospheric Sciences, and Guangdong Province Key Laboratory for Climate Change and Natural Disaster Studies, Sun Yat-sen University, Zhuhai, China

[5] Department of Geological Sciences, Jackson School of Geosciences, The University of Texas at Austin, Austin, TX, USA

[6] Southern Marine Science and Engineering Guangdong Laboratory (Zhuhai), Zhuhai, China

Submitted to Journal of Geophysical Research

April 2021

Key Points:

- Anthropogenic heat creates higher CAPE and lower CIN in urban locations within the Pearl River Delta and intensifies urban extreme rainfall
- Global warming results in higher CAPE which exacerbates extreme rainfall in both

urban and surrounding rural areas

- Impacts due to intense anthropogenic heat and global warming on extreme rainfall can be comparable over highly urbanized coastal locales

Keywords:

Extreme rainfall, anthropogenic heat flux, global warming, climate change

Corresponding author address: Dr. Chi Yung Francis Tam, Earth System Science Programme, The Chinese University of Hong Kong, Hong Kong. Email: Francis.Tam@cuhk.edu.hk

Abstract

This study compares the impacts of global warming and intense anthropogenic heat (AH) on extreme hourly precipitation over the Pearl River Delta (PRD) megacity, located in coastal South China. Using the cloud-resolving Weather Research and Forecasting (WRF) model coupled with the single-layer urban canopy model (SLUCM), three downscaling experiments were carried out: the first (second) having zero (300W/m^2 as diurnal maximum) AH values prescribed over PRD urban grids, under the same current climate conditions. The third experiment with AH=300W/m^2 under future projected climate representative concentration pathway (RCP) 8.5. Boundary conditions were derived from PRD extreme rainfall episodes, identified from the Geophysical Fluid Dynamics Laboratory Earth System Model (GFDL-ESM2M) historical and RCP8.5 runs. Global warming forcing leads to ~20 to more than 100% increase in the probability of hourly precipitation with the magnitude of 20-100mm/hr over urban locations. The enhancements from intense AH forcing were similar. However, two types of forcings have distinct signatures in modulating the thermodynamic environment. Warming due to AH is limited to the lowest 1km above ground, while global warming warms up the whole troposphere. Intense AH results in enhanced convective available potential energy (CAPE) and reduced convective inhibition (CIN) within the megacity, allowing convection to be triggered more easily and with more vigor. On the other hand, global warming enhances both CAPE and CIN, over both urban and rural areas. Our results highlight the different physical mechanisms of AH and global warming in exacerbating extreme urban rainfall, despite their having similar impacts on the rainfall intensity.

1. Introduction

The Pearl River Delta (PRD) is located in the Greater Bay Area of the southern coast of China with a subtropical climate. During summer, weather and circulation elements such as troughs of low pressure, southwest monsoon, tropical cyclones, and severe thunderstorm systems can bring widespread or localized heavy rainfall to the region (Heywood, 1953; Bell, 1969; Wai et al., 1995; Luo et al., 2017). In the past few decades, PRD has seen very rapid urbanization; for instance, the proportion of built-up urban areas in the region has quadrupled from the year 1990 to 2010 (Du et al., 2013). Urbanization is known to influence the local meteorology by modifying land-surface properties (Bornstein, 1968; Carlson et al., 1981; Oke, 1988; Sisterson and Dirks, 2015), including the introduction of urban morphology (Oke, 1981; Kusaka el al., 2001; Coceal and Belcher, 2004; Shepherd, 2005). Previous works such as those from the Metropolitan Meteorological Experiment (METROMEX; Huff and Changnon, 1973) and by others (Han et al., 2014; Liang and Ding 2017; Liu and Niyogi 2019), indicate that the urban heat island (UHI) effect can enhance precipitation over cities. Bornstein and Lin (2000) concluded that this is due to UHI-induced convergence (see also Rozoff et al., 2003). Being an essential contributor to UHI, the anthropogenic heat (AH) flux also affects urban rainfall (Nielsen et al., 1981; Oke, 1988; Wilby et al., 2009). A recent study also shows that intense urban rainfall is more sensitive to AH than land cover changes over the PRD region (Hu et al., 2021).

At the same time, a substantial increase of extreme daily and hourly rainfall intensity over southern China and PRD has been observed in the past 60 years (Zhang et al., 2009; Wong et al., 2010; Hartmann, 2013). Different climate projections also estimate that, under a warmer climate, the occurrence of light rain (1 – 10 mm/day) would be suppressed while that of heavy rain would be enhanced (Chou et al., 2012; Ueda et al., 2006; Qian et al., 2007; Lee et al., 2011). The intensification of extreme precipitation is likely related to the enhancement

of maximum moisture content in the atmosphere, broadly following the Clausius-Clapeyron (CC) relation of ~7% increase per degree K rise in lower tropospheric temperature. Indeed, rising extreme rainfall amplitudes conforming to the CC (or even super-CC) relation over locations with different background climate, such as Hong Kong and the Netherlands, have been reported (Lenderink et al., 2011).

Over the urban areas, both urbanization and global warming can contribute to heavy rainfall intensification. Georgescu et al. (2021) conducted a modeling study showing that urban expansion can either enhance or suppress extreme rainfall, while global warming can compensate the effect of urban expansion, giving a net enhancement in extreme rainfall over continental US. Holst et al. (2016, 2017) and Hu et al. (2021) used a cloud-resolving atmospheric model to examine the sensitivity of precipitation intensity to the level of AH over PRD. Based on simulations for a record-breaking historical case (Holst et al.) or extreme cases from model outputs (Hu et al.), it was found that the presence of AH can significantly enhance the probability of heavy rainfall in urban locations. Hu et al. (2021) also showed that the enhancement of AH on extreme rainfall is stronger than land cover changes, which is consistent with the weak response from urban expansion concluded by Georgescu et al. (2021). As global warming and local urbanization are the main contributing factors to the long-term increase of local temperature in the region (Lee et al., 2011; Chan et al., 2012), it is of interest to further compare such AH impacts with those due to a warming climate on extreme precipitation.

This study seeks to address this issue based on a methodology similar to that used by Holst et al. (2016, 2017) and Hu et al. (2021), again focusing on the PRD region. In order to examine the impacts of global warming, extreme rainfall cases simulated by a coarse-resolution General Circulation Model (GCM), for both the present and future projected climate were dynamically downscaled using a high-resolution model. Furthermore, during the

downscaling exercise for both the historical run and future climate projections, various values of AH within the PRD megacity area were prescribed to investigate the sensitivity of heavy precipitation to urban heating. The rest of this paper is organized as follows. Section 2 describes the model and experimental setup. Results on different impacts on the urban rainfall characteristics and thermal environment due to AH and global warming are given in section 3. Concluding remarks can be found in section 4.

2. Model experimental design and AH flux

For conducting downscaling experiments with a focus on the PRD megacity, the Weather Research and Forecast (WRF) model version 3.8.1, with Advanced Research WRF (ARW) dynamic core (Skamarock et al., 2008), coupled with a single-layer urban canopy model (SLUCM) (Kusaka and Kimura, 2004) was employed to dynamically downscale outputs from the Geophysical Fluid Dynamics Laboratory (GFDL) Earth System Model (GDFL-ESM2M; Dunne et al., 2012, 2013). Here we used the Noah Land Surface Model (Noah LSM; Tewari et al., 2004), which supports SLUCM in WRF. Other physical parameterizations include the Rapid Radiative Transfer Model for GCMs (RRTMG) for long-wave radiation (Iacono et al., 2008), the short-wave radiation scheme by Dudhia (1989), the single-moment 6-class microphysics scheme (Hong and Lim, 2006), the planetary boundary layer scheme by Bougeault and Lacarrere (1989), and also the simplified Arakawa-Schubert cumulus scheme (outermost domain only; Pan and Wu, 1995). Figure 1 shows the three nested model integration domains, with the horizontal grid spacing of 50 km (129×89) in the outermost (d01), 10 km (70×80) in the middle (d02) and 2 km (130×130) in the innermost domain (d03), which is a convection-permitting resolution. One-way nesting was employed, and there are 39 vertical levels with a prescribed model top at 30 hPa. Land surface is categorized according to Moderate Resolution Imaging Spectroradiometer (MODIS) data in WRF for all scenarios.

To identify extreme precipitation events in the present and future climate, the GFDL-ESM2M 1946 to 2005 historical run, as well as the RCP8.5 projection from 2039 to 2099, were examined. McSweeney et al. (2015) studied 28 Coupled Model Intercomparison Project Phase 5 (CMIP5) models and concluded that the GFDL earth system models could give satisfactory circulation features over South East Asia. Figure 2 shows the May-to-September (MJJAS) rainfall climatology from GFDL-ESM2M historical run data covering 1945 to 2005, and also that based on the Tropical Rainfall Measuring Mission (TRMM) multi-satellite 3B42 products from 1998 to 2013 (Huffman et al., 2014). Overall, it can be seen that the broad-scale precipitation features over East Asia, such as the Meiyu-Baiu rainband from Eastern China extending into Japan, are reasonably captured. Over South China, there is a slight underestimation of rainfall intensity over the coastal area. A more detailed model evaluation of the meteorology, including wind, temperature and pressure, also shows that GFDL-ESM2M has satisfactory performance over Southeast Asia (Fung, 2018).

Prior to selecting the extreme episodes, probability distribution functions (PDF) of daily mean precipitation products, averaged over the South China region of 17–27^{o}N, 105–117^{o}E, were computed. For both climate runs, extreme events were identified whenever the daily rainfall averaged over this region reaches the 99th percentile (R99p) threshold or above in their own climates. It was found that ~ 75% of identified cases occur within the MJJAS period (see Figure 3); this is the case in TRMM observations, the GFDL-ESM2M historical as well as RCP8.5 simulations. By inspection, some of these episodes are clearly related to tropical cyclone (TC)-like systems in the GFDL-ESM2M runs; these systems are not considered here. For each climate scenario, at least 17 non-TC events out of 70 extreme cases within MJJAS were dynamically downscaled by WRF-SLUCM, with integration starting from three days prior to the rainfall peak and lasting for at least 6 days. Spectral nudging (with wavelengths of ~ 1300 km or above for the meridional and zonal wind variables at

levels above 500 hPa; see Lo et al., 2008) was applied to the outermost domain of the WRF model to ensure the consistency of synoptic conditions between WRF-SLUCM simulations and GFDL-ESM2M boundary forcing. As illustrated in Figure S2 for a selected case, the spectral nudging method can substantially improve the timing and location of heavy precipitation reproduced by WRF-SLUCM. Based on 26 selected R99p cases statistics, spectral nudging can minimize the rainfall intensity error in South China by over 20%.

Finally, for SLUCM parameters adopted for the WRF model integrations, default values were used, except for AH (see below), average building height (set to 30.0 m), and road width (16.0 m). Values for the latter two parameters were based on data relevant to the city of Hong Kong (see Hong Kong Planning Standards and Guidelines, https://www.pland.gov.hk/pland_en/tech_doc/hkpsg/full/ch8/pdf/ch8.pdf). Oke (1988) reported a diurnal AH peak of about 1200 W m^{-2} during summer days at a highly urbanized location in Hong Kong. A more recent study based on satellite measurements gives a diurnal peak of ~289 (283) W m^{-2} in summer (winter), averaged over all urban locations within Hong Kong (Wong et al., 2015). A typical workday AH profile for a city reaches peaks in the morning and evening due to the emission from transportation, buildings, and other anthropogenic activities (Oke, 1988; Ichinose et al., 1999; Flanner, 2009; Allen et al., 2011; Sailor, 2011). In this study, a diurnal profile of AH with peaks at 7 am and 4 pm local time (Figure S1) was imposed in the SLUCM (see Holst et al., 2016; Hu et al., 2021).

To assess the impacts of AH, parallel experiments, one with the peak value of 300 W m^{-2} (with daily average of 160 W m^{-2}), and one with AH equal to zero, were conducted. The former setting corresponds to the scenario in which every urban grid point in PRD has a condition similar to Hong Kong city area. Note that the peak (daily average) of 300 (160) W m^{-2} used for all urban PRD locations should be considered as pertaining to a "high urbanization" scenario. Three different global AH datasets were used as reference to evaluate

the validity of AH values adopted here, namely those from Flanner (2009), Jin et al. (2020) and Yang (2017). The datasets were derived from different algorithm and combination of energy consumption, population, night-time light, impervious surface coverage and normalized difference vegetation index. After re-gridding to 2 km x 2 km resolution (i.e., same as that for the WRF-SLUCM innermost domain), the maximum AH magnitudes in Hong Kong are 154, 289, and 76 W m^{-2} in the Flanner, Jin et al., and Yang datasets, respectively (see Figure S3). The result indicates that the choice of daily mean AH of 160 W m^{-2} falls within a reasonable range of values.

Altogether, there are three sets of downscaling experiments conducted using WRF-SLUCM: one with zero AH and one with peak AH = 300 W m^{-2} in the historical climate (1946-2005), hereafter referred to as HIST_AH0 and HIST_AH300, respectively, and the same peak AH = 300 W m^{-2} settings but for the 2039-2099 period according to the RCP8.5 scenario (referred to as RCP85_AH300). Here the impacts of AH, valid for the present climate, can be inferred by comparing HIST_AH300 with HIST_AH0, while and the influence of global warming for a highly urbanized PRD region can be assessed by comparing RCP85_AH300 with HIST_AH300 outputs.

3. Results

3.1. Rainfall statistics over South China

The daily rainfall statistics of GFDL-ESM2M historical and RCP8.5 scenarios over South China were first investigated (Figure 4). It can be seen that, in the historical climate and RCP8.5 scenario, the 99th percentiles (R99p) of daily mean precipitation rates are 16.8 mm day^{-1} and 18.4 mm day^{-1}, respectively. There is an enhancement of about 9.5% of the extreme rainfall intensity in the future climate, according to RCP8.5. The PDFs also show that the 95th percentile of daily rainfall and the simple daily intensity index (SDII, defined as

the total accumulated rainfall divided by the number of rain days) are projected to increase by 5.8% and 4.5%, respectively. We have also examined the occurrence frequency of extreme cases in different climate simulations by adopting the same threshold value of 16.8 mm day^{-1} (i.e., the R99p value from the historical run). It was found that under RCP8.5, the frequency of extreme events can increase up to ~52% compared to the present climate. Overall, it is clear that extremely precipitation rates, or the frequency of extreme episodes, are projected to increase over South China, based on the GFDL-ESM2M simulations.

The outputs from WRF-SLUCM simulations were then examined, focusing on the PRD heavy precipitation. To ensure that the simulations can well capture the rainfall characteristics, rain rate PDFs from 50km x 50km WRF-SLUCM simulations (the outermost domain d01) are first compared with those from GFDL-ESM2M. These PDFs were computed using the daily mean precipitation data over the PRD area, aggregated throughout the meso-scale model integration and all non-TC cases (see section 2). In general, there is reasonable agreement between the behavior of downscaled precipitation and that from the parent model, for both the historical and RCP8.5 climate runs (see Figure S4).

3.2. Intense AH and global warming influences on extreme hourly rainfall statistic

The intense AH impacts on extreme hourly rainfall over the PRD megacity were examined in the innermost model domain (d03) of the WRF-SLUCM outputs. Figures 5a shows the hourly rain rate PDFs over urban grids, from the HIST_AH0 and HIST_AH300 experiments, respectively. It can be seen that the presence of intense AH can enhance the frequency of heavy rain in urban areas, as indicated by the increase of probability for rain rates $\geq$ 10 mm hr^{-1} in the HIST_AH300 run. As such, the frequency for lighter rain (< 10 mm hr^{-1}) is reduced in comparison with HIST_AH0. The presence of AH also enhances the total rainfall by ~7% over the whole PRD area. We have also examined how the rain rate PDF is shifted due to AH over each grid point in d03. Kolmogorov–Smirnov (KS; Smirnov, 1948)

tests showed that, over the highly urbanized inland locations over the northwestern part of the domain (from 133 to 134°E, centered at 23°N), the distributions are distinct from each other at the 90% confidence level (see Figure 6a). Inspection of each individual event revealed an increase in the probability of rain in more than 90% of these downscaled cases, comparing the HIST_AH300 with the HIST_AH0 runs. The above results are consistent with those of Holst et al. (2016) and Hu et al. (2021), who showed that heavy rainfall intensity is indeed sensitive to AH based on model simulations. The impacts of global warming effect under intense AH conditions are shown in Figure 5b. Overall, the probability of heavy rain ($\geq$ 10 mm hr^{-1}) is enhanced, while that for light rain (< 10 mm hr^{-1}) is reduced over the urban area due to a warmer background climate. In comparison with the effect of AH, global warming influences a broader region, with more than 50% of both urban and non-urban locations in d03 showing a significant change in the rainfall PDF (see Figure 6b for results of KS tests). There is also ~3% increase of the accumulated rainfall over all the downscaled cases in the whole PRD, comparing the RCP8.5 and historical climate simulations, which is slightly less than the AH effect (7%).

To compare the influence of AH and global warming, Figures 5c and 5d show the fractional change of the PDFs for both urban and non-urban grids, respectively. The impact of AH is localized over the urban area, with fractional enhancements from ~ 20% at 10 – 20 mm hr^{-1} to ~ 165% at 80 – 90 mm hr^{-1} (see orange bars in Figure 5c). Over non-urban regions, AH has very little impact on the precipitation characteristics (green bars). Regarding global warming's effect, there is also a clear increase of probability of heavy rain, by ~ 10% (for 20 – 30 mm hr^{-1}) to ~ 170% (for 70 – 80 mm hr^{-1}), over urban area in PRD (see orange bars in Figure 5d). It is noteworthy that, in a warmer climate, the probability of occurrence of intense rainfall increases in both urban and non-urban sites. Finally, in terms of how extreme rainfall frequency is affected, the AH and global warming effects are comparable.

3.2. Mechanisms of AH and global warming impacts

To investigate the mechanisms through which the regional rainfall characteristics are changed, Figure 7a shows the 2-m temperature difference between the HIST_AH300 and the HIST_AH0 experiments, averaged over all simulation cases and throughout their integration periods. It is seen that AH can enhance the urban surface temperature up to about 2 K; over non-urban regions, the enhancement is small (about 0.14 K). Thus, there is 2 K temperature difference between the highly urbanized locations in PRD and the peripheral rural areas due to the presence of AH. The localized temperature increment showed a pattern similar to that by Zhang et al. (2019) and Hu et al. (2021). On the other hand, global warming effect increases the 2-m temperature of the cases ensemble by ~2.2 K uniformly over the whole model domain (see Figure 8a). The vertical structure of the temperature change is also examined, by taking the average over urban and non-urban grid boxes separately for each set of experiments (see Figure 7b). Temperature anomalies due to the presence of AH are confined to the lowest 1km above the ground (cyan and blue curves in Figure 7b). In comparison, under a warmer background climate, there is anomalous warming throughout the atmospheric column, as expected from global warming experiments (see red and cyan curves in Figure 7b).

Figures 7c and 7d respectively give the change of convection available potential energy (CAPE) and convective inhibition (CIN) due to the presence of AH. AH can significantly enhance CAPE (by ~14%) and can also reduce CIN (by ~14%) over the urban area, which is opposite to Zhang et al. (2019)'s conclusion. Thus, the warmer near-surface temperature provides more potential energy, and at the same time, a more unstable environment for strong convection to take place over the megacity. It is noteworthy that CIN in the sub-urban area is increased, implying a non-local effect of AH. This is probably related to the induced local overturning circulation, with rising (sinking) motion over the urban (non-

urban) regions (see Figure 9). A warming zone up to ~1 km above the megacity can be found (red contours in Figure 9b); such a thermal structure is conducive to more intense convection in urban locations (Figure 5c). On the other hand, global warming impact on CAPE and CIN is markedly different. While CAPE is increased over the whole model domain (by ~20%) (see Figure 8a), there is no significant change of CIN over the urbanized PRD land area (Figure 8b). The decrease of CIN (Figure 8c) is found only over oceanic regions, due to a warmer background climate. This is likely related to the warmer regional SST in the GFDL-ESM2M future climate projection, which gives rise to a more unstable environment (Figure 8a). Overall, these results highlight the strong influence of AH on extreme precipitation in megacities, and that a careful treatment of urban physics, in particular the low-level temperature profile, is needed when simulating and projecting heavy rainstorms over urban areas in the future climate.

4. Discussions and Summary

We have assessed the impacts of AH and global warming on the characteristics of extreme precipitation over PRD, by dynamical downscaling of heavy rainfall episodes from the GFDL-ESM2M simulations using WRF-SLUCM. In particular, the GFDL-ESM2M present climate run and RCP8.5 future projection was used; for each scenario, parallel experiments with zero AH and with AH set to 300Wm^{-2} (as the daily maximum) within the megacity area were conducted. It was found that the presence of AH enhances the probability of heavy rainfall (> 10 mm hr^{-1}) in urban locations, consistent with the enhanced rainfall by AH concluded in Hu et al. and Holst et al. Moreover, the fractional increment of probability increases with the rainfall intensity, from ~ 20 % at 10 – 20 mm hr^{-1} to ~ 165 % at 80 – 90 mm hr^{-1}, showing a shift of rainfall to the extreme tail side.

Georgescu et al. (2021) evaluated the effects of global warming and urban expansion

on extreme rainfall based on simulations at 20-km spatial resolution. This study uses WRF at the convection-permitting resolution of 2 km, which can better represent the urban surface processes and atmospheric physics. Heavier precipitation is likely related to the rise of surface temperature over urban locations, which is about 1.8 K when averaged over all episodes examined. This in turn enhances (reduces) CAPE (CIN) in the urban area, which is conducive to strong convection. On the other hand, there is no significant change of heavy rainfall over non-urban locations due to the presence of AH. In comparison, global warming is seen to have an impact on precipitation characteristics over the whole PRD, with the enhancement of both urban and non-urban heavy rainfall probability, which is consistent with Georgescu et al. (2021) modeling results in the continental US. Compared with the present climate (1946-2005), on average, there is about 2.3 K increase of surface temperature in PRD for the RCP8.5 (2039-2099) downscaled cases, and CAPE is increased by ~ 20 % uniformly within the region. It is striking that, over the megacity area, the enhancement of extreme precipitation due to intense AH is comparable to that due to global warming. However, the two effects are due to different mechanisms, as suggested by their different impacts on the regional circulation and values of CIN.

The current urban canopy model (UCM) setup is based on the MODIS 2002 land use categorization; the latter can be updated to reflect urban development over PRD in recent years. Moreover, the same set of urban parameters, based on the urbanization condition in Hong Kong, was used in the SLUCM throughout the whole innermost model domain; this might not reflect the spatial heterogeneity of AH, building morphology and building materials in the PRD region. More up-to-date urban land surface information with finer classification, such as those from the World Urban Database and Access Portal Tools (WUDAPT) can be utilized (Ching et al., 2018; Wang et al., 2019), in order to assess more realistically how urban heating, or other physical characteristics in relation to urban landuse,

might affect the local extreme rainfall, such as anthropogenic aerosols. Also, our results presented here depend on outputs from a single GCM, namely the GFDL-ESM2M; future climate projections from more models and different greenhouse gas emission scenarios (e.g., RCP4.5 and RCP6.0) can be downscaled dynamically, so as to better sample uncertainties due to the use of different GCMs and emission scenarios. Finally, the same downscaling method can be adopted to examine other types of inclement weather, such as heat waves and tropical cyclones, and their influence on the urban environment. More studies have to be carried out to investigate how global warming might affect various types of extreme events, and their interactions with megacities under the foreseeable future land use and urban development together with global warming.

Acknowledgements.

The Weather Research and Forecasting model is downloaded from (https://www2.mmm.ucar.edu/wrf/users/download/get_source.html). The GFDL-ESM2M data are acquired from the GFDL local server (http://nomads.gfdl.noaa.gov:8080/DataPortal/cmip5.jsp). The TRMM-3B42 rainfall estimate product is downloaded from (https://doi.org/10.5067/TRMM/TMPA/3H/7). The high−performance computation was supported by Information Technology Services Centre of the Chinese University of Hong Kong. We thank Joong-Bae Ahn, Mat Collins, Gabriel Lau, Song Yang, P.W. Chan, S.M. Lee, C.M. Shun and Zong-Liang Yang for discussions. This work is jointly supported jointly by the National Key Research and Development Program of China (Ref. No. 2019YFC1510400), the Hong Kong Research Grant Council's Early Career Scheme (No. 104712), General Research Fund (No. 14308017), the Pearl River S&T Nova Program of Guangzhou (No. 201906010054) and Shenzhen Research Institute, the Chinese University of Hong Kong (Grant No. A.02.20.00401).

Figure captions

Figure 1. Nested model domains d01, d02, d03 adopted for dynamical downscaling and the urban landuse coverage over PRD based on MODIS data (red shading) in d03.

Figure 2. Climatological mean distribution of the occurrence of extreme rainfall cases in South China identified based on the 99th percentile threshold in the GFDL-ESM2M historical run (blue), the RCP8.5 climate scenario (red) and TRMM-3B42 (black). ~ 75% cases in both climates are found in May-to-September period.

Figure 3. PDFs of daily rainfall averaged over South China (17ºN – 27ºN, 105ºE – 117ºE) from the GFDL-ESM2M historical (blue) and RCP8.5 (red) climate simulations. Dotted lines indicate the values corresponding to the 99th percentile. Shaded areas represent the top 1 percentile of the cumulated distributions.

Figure 4. PDFs of daily rainfall averaged over South China (17°N – 27°N, 105°E – 117°E) from the GFDL-ESM2M historical (blue) and RCP8.5 (red) climate simulations. Dotted lines indicate the values corresponding to the 99th percentile. Shaded areas represent the top 1 percentile of the cumulated distributions.

Figure 5. (a, b) PDFs of hourly rain rates in the ranges of 0-10, 10-20, 20-30, 30-40, 40-50, 50-60, 60-70, 70-80, 80-90, 90-100 and 100-110 mm hr^{-1} in d03, computed based on outputs over all urban grids by downscaling non-TC heavy rainfall cases from the GFDL-ESM2M historical run with zero AH (cyan), historical run with peak diurnal AH = 300 W m^{-2} (blue) and RCP8.5 simulations with peak AH = 300 W m^{-2} (dark red). (c, d) Fractional change of hourly rain rate probability due to AH effect over urban (orange) and non-urban grids (green) in d03. (d) Same as (c) except for gauging global warming effect. See text for details.

Figure 6. KS test between (a) HIST_AH300 and HIST_AH0 and (b) RCP85_AH300 and HIST_AH300. The dotted regions indicated that p-value < 0.1.

Figure 7. (a) 2-m temperature, (c) convective available potential energy (CAPE) and (d) convective inhibition (CIN) difference between WRF-SLUCM outputs with peak AH of 300 W m-2 from those with peak AH set to zero, by downscaling the GFDL-ESM2M historical run. (b) Vertical temperature profiles averaged over urban grids in d03 for downscaled historical run with zero AH (cyan), historical run with diurnal peak AH = 300 W m-2 (blue), and RCP8.5 simulations with peak AH = 300 W m-2 (red). All values are computed by time averaging downscaled results from d03 and by averaging the selected non-TC heavy rainfall cases identified in the GFDL-ESM2M simulations. See text for details. Units of CAPE and CIN: J kg-1.

Figure 8. (a) 2-m temperature, (b) CAPE and (c) CIN difference between GFDL-ESM2M RCP8.5 and historical run downscaled by WRF-SLUCM with peak AH of 300 W m^{-2}. All values are computed by time averaging downscaled results from d03, and by averaging over selected of non-TC heavy rainfall cases identified in the GFDL-ESM2M simulations. See text for details. Units of CAPE and CIN: J kg^{-1}.

Figure 9. Vertical cross section plot of wind circulation (vectors) and vertical wind speed (shaded) anomaly of downscaled non-TC extreme cases with prevailing wind direction in N – S. (a) labelled the cross-section line, (b) is the anomaly plot of AH effect at GFDL-ESM2M historical run (HIST_300 – HIST_0).

List of figures

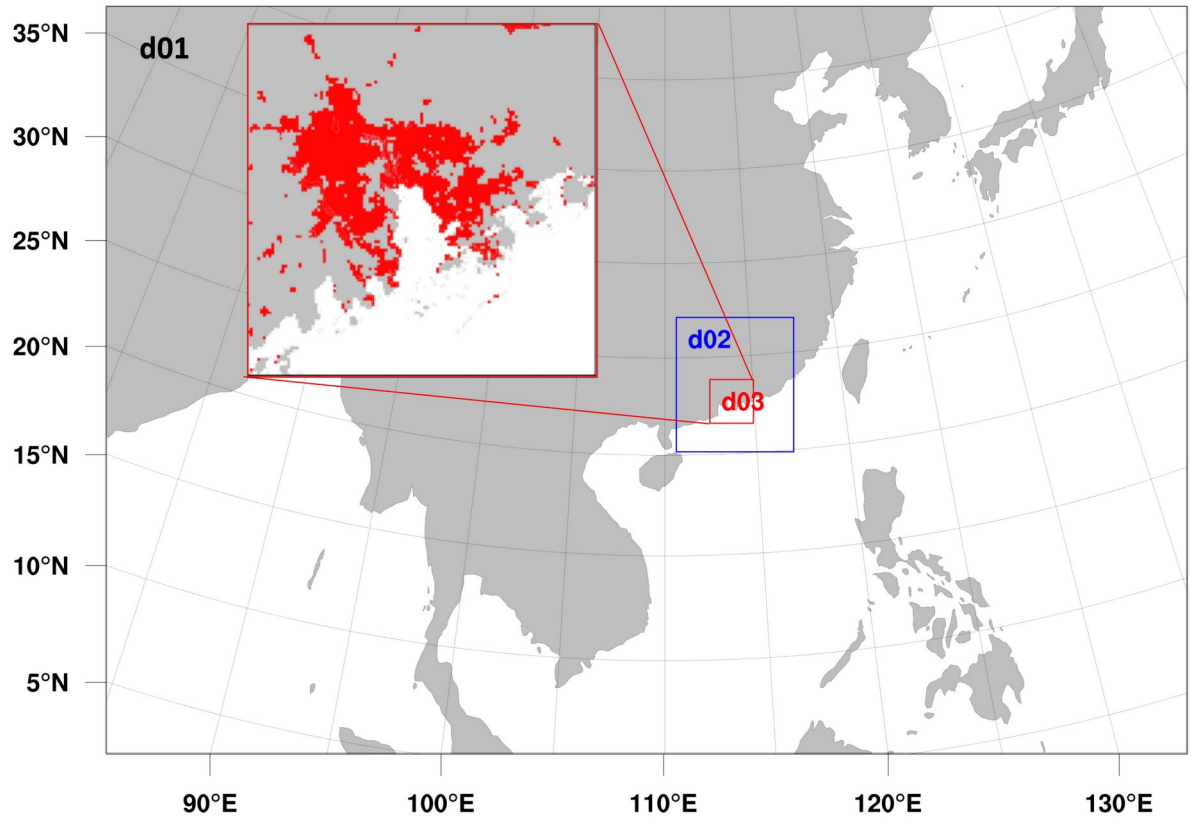

Figure 1. Nested model domains d01, d02, d03 adopted for dynamical downscaling and the urban landuse coverage over PRD based on MODIS data (red shading) in d03.

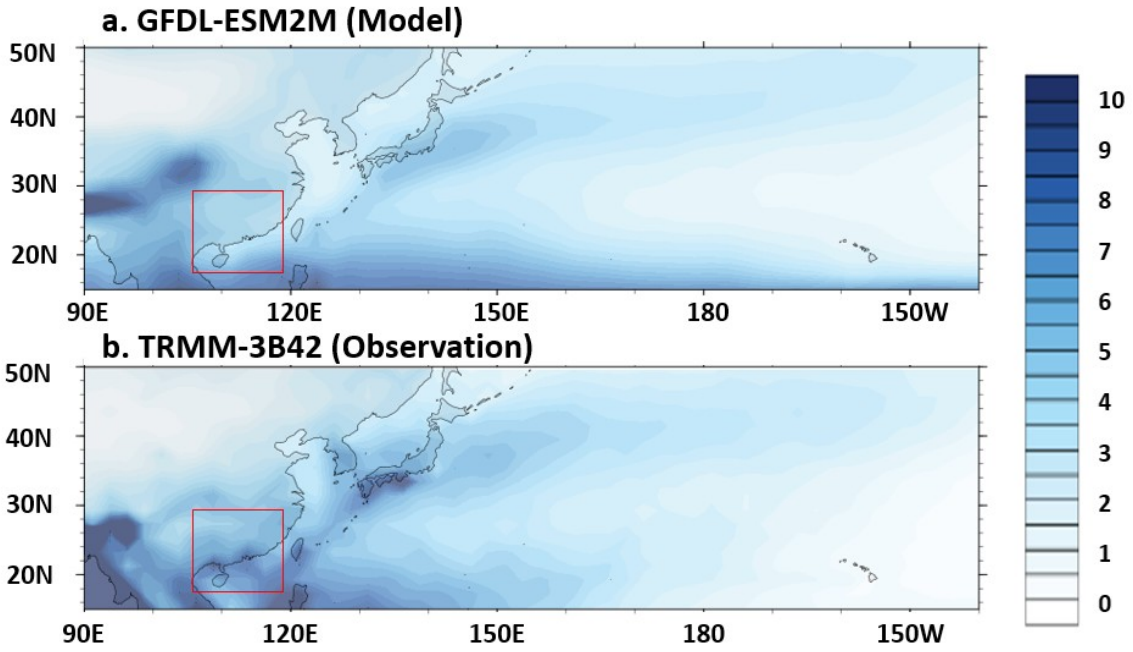

Figure 2. The climatological daily rainfall of May to September from (a) GFDL-ESM2M historical climate scenario (1946-2005) and (b) TRMM-3B42 (1998-2013). The red box marked the South China region (17-27°N, 105-117°E).

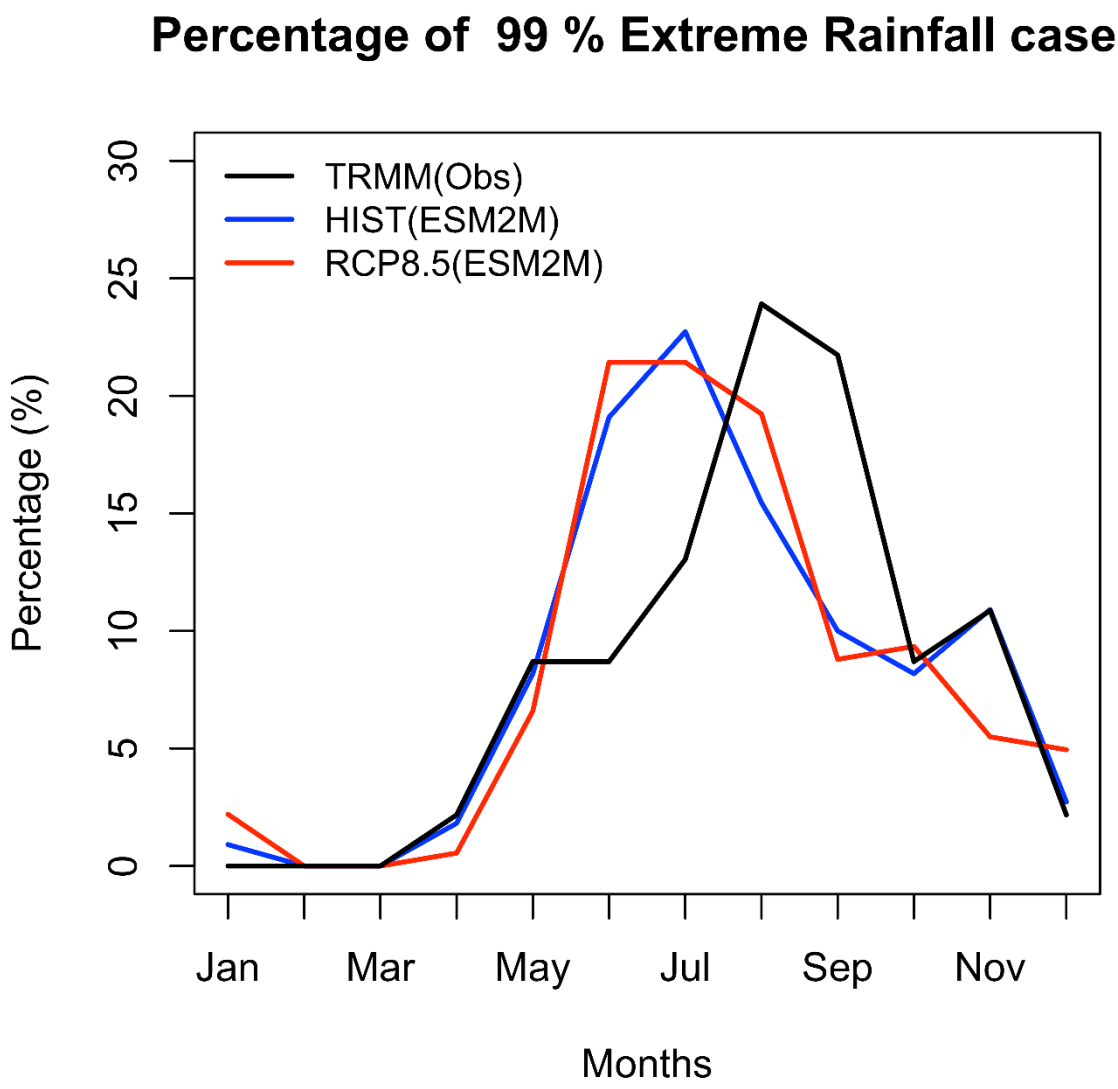

Figure 3. Climatological monthly distribution of the occurrence of extreme rainfall cases in South China identified based on the 99th percentile threshold in the GFDL-ESM2M historical run (blue), the RCP8.5 climate scenario (red) and TRMM-3B42 (black). ~ 75% cases in both climates and TRMM-3B42 are found in the May-to-September period.

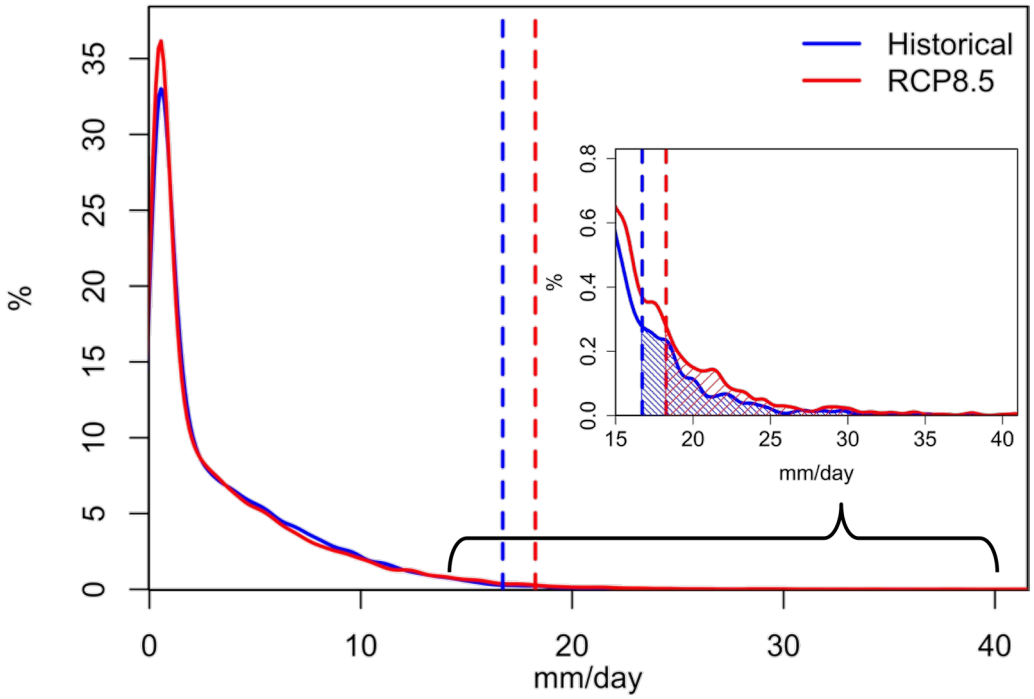

Figure 4. PDFs of daily rainfall averaged over South China (17°N – 27°N, 105°E – 117°E) from the GFDL-ESM2M historical (blue) and RCP8.5 (red) climate simulations. Dotted lines indicate the values corresponding to the 99th percentile. Shaded areas represent the top 1 percentile of the cumulated distributions.

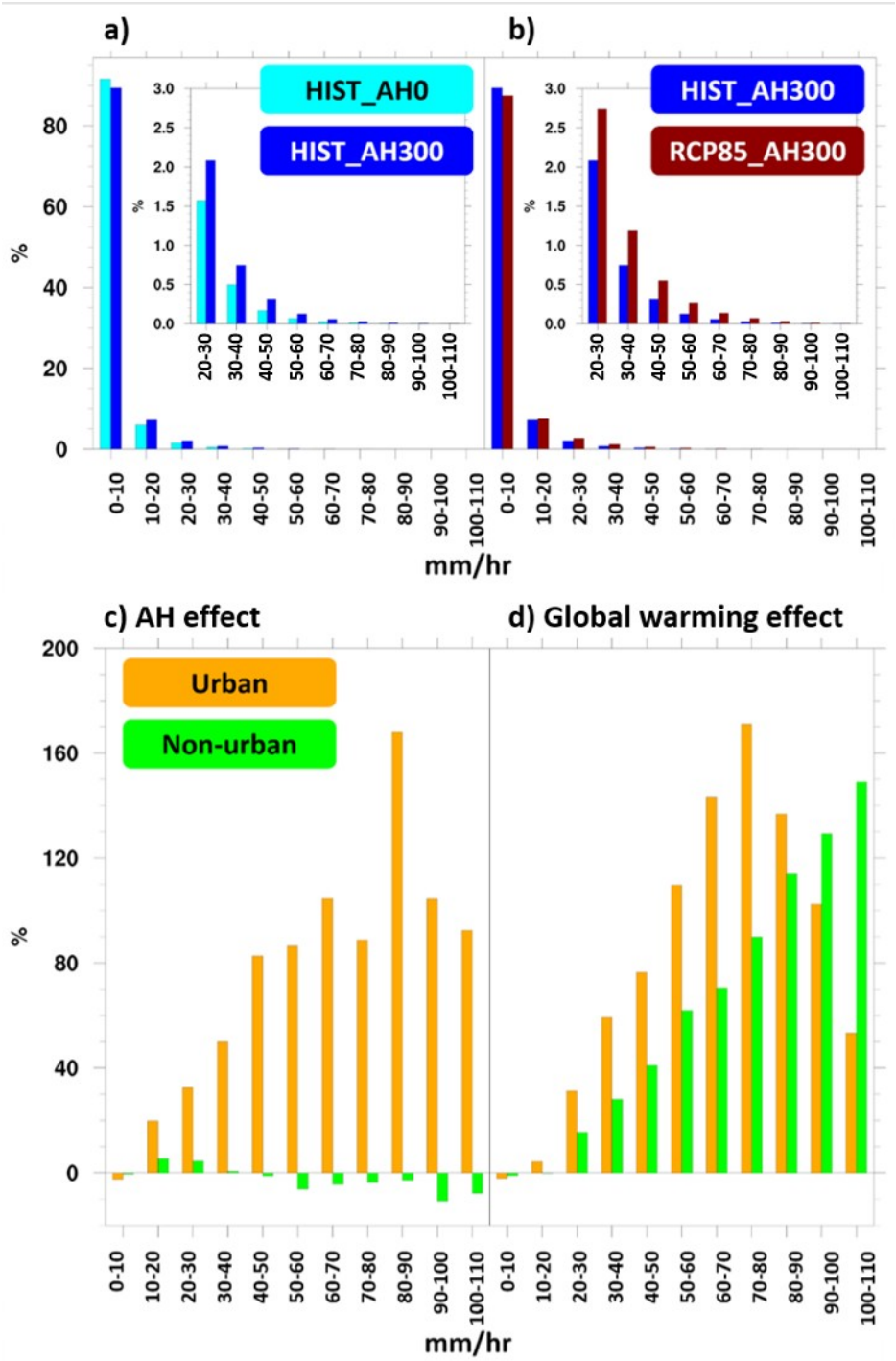

Figure 5. (a, b) PDFs of hourly rain rates in the ranges of 0-10, 10-20, 20-30, 30-40, 40-50, 50-60, 60-70, 70-80, 80-90, 90-100 and 100-110 mm hr^{-1} in d03, computed based on outputs over all urban grids by downscaling non-TC heavy rainfall cases from the GFDL-ESM2M historical run with zero AH (cyan), historical run with peak diurnal AH = 300 W m^{-2} (blue) and RCP8.5 simulations with peak AH = 300 W m^{-2} (dark red). (c, d) Fractional change of hourly rain rate probability due to AH effect over urban (orange) and non-urban grids (green)

in d03. (d) Same as (c) except for gauging global warming effect. See text for details.

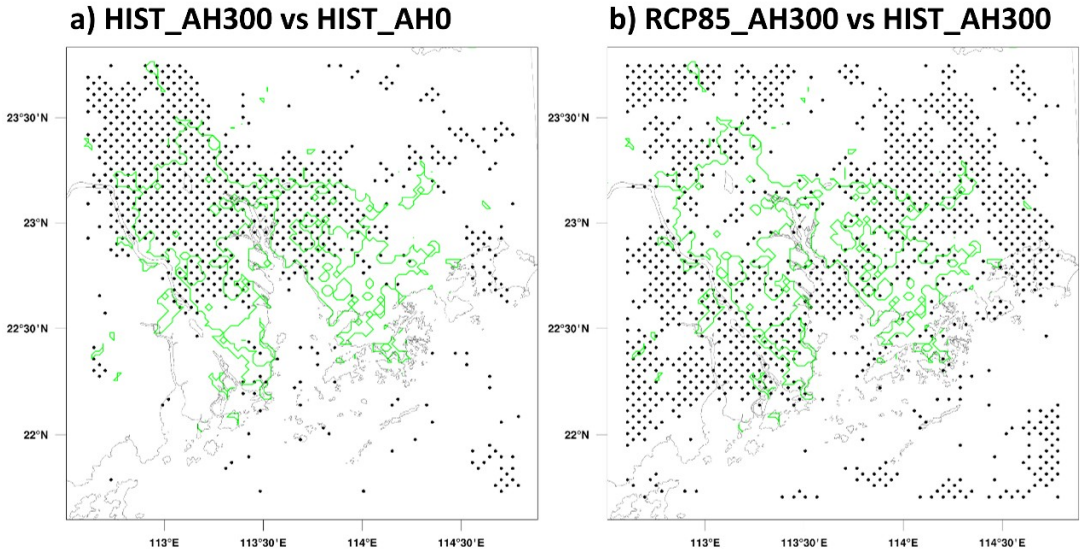

Figure 6 KS test between PDFs of (a) HIST_AH300 and HIST_AH0, and PDFs of (b) RCP85_AH300 and HIST_AH300. The dotted regions indicated that p-value < 0.1.

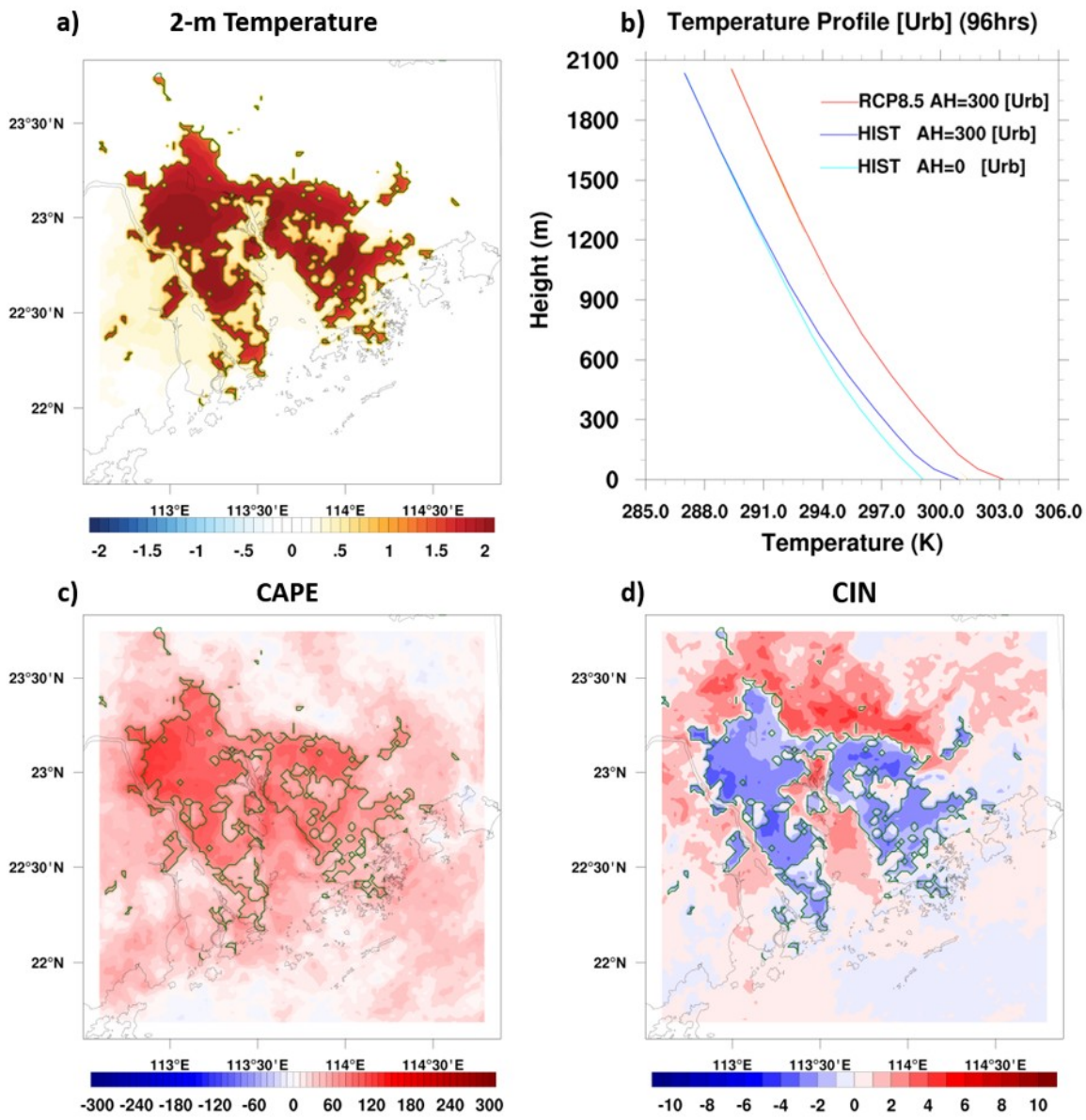

Figure 7. (a) 2-m temperature, (c) convective available potential energy (CAPE) and (d) convective inhibition (CIN) difference between WRF-SLUCM outputs with peak AH of 300 W m^{-2} from those with peak AH set to zero, by downscaling the GFDL-ESM2M historical run. (b) Vertical temperature profiles averaged over urban grids in d03 for downscaled historical run with zero AH (cyan), historical run with diurnal peak AH = 300 W m^{-2} (blue), and RCP8.5 simulations with peak AH = 300 W m^{-2} (red). All values are computed by time averaging downscaled results from d03 and by averaging the selected non-TC heavy rainfall cases identified in the GFDL-ESM2M simulations. See text for details. Units of CAPE and CIN: J kg^{-1}.

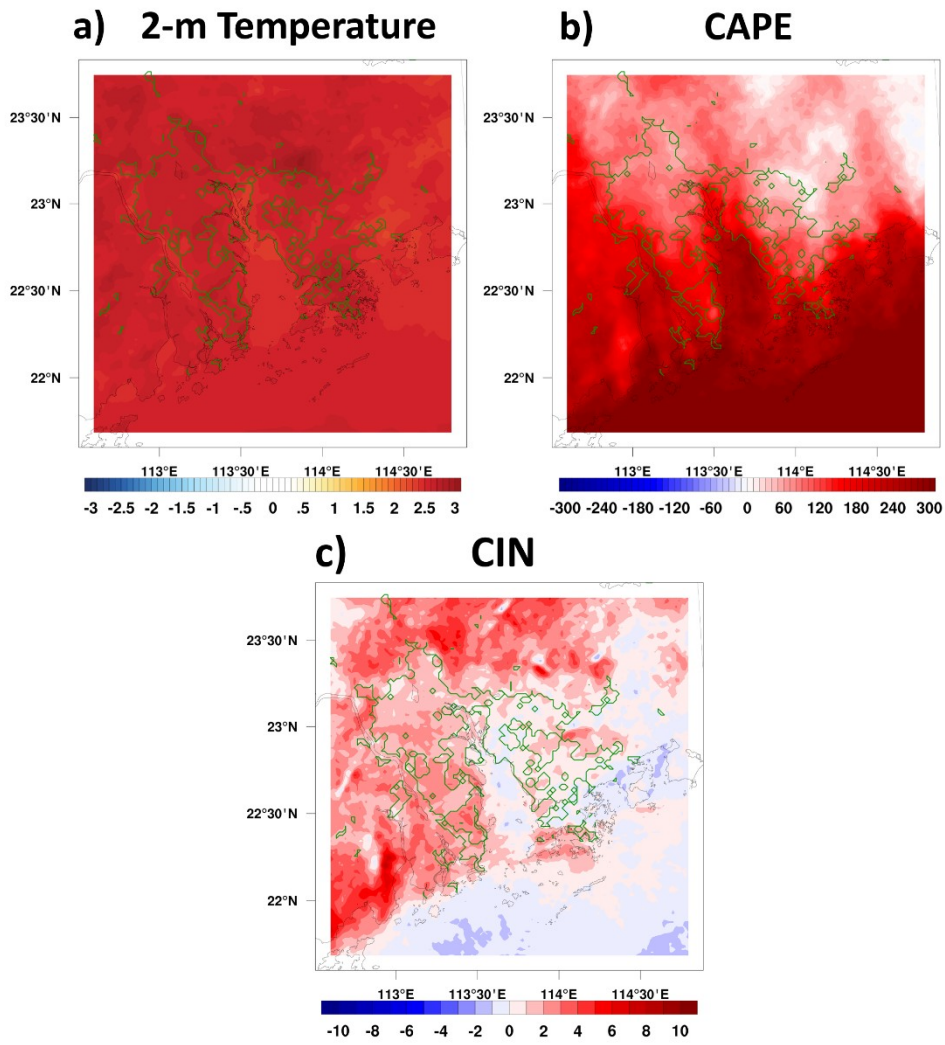

Figure 8 (a) 2-m temperature, (b) CAPE and (c) CIN difference between GFDL-ESM2M RCP8.5 and historical run downscaled by WRF-SLUCM with peak AH of 300 W m^{-2}. All values are computed by time averaging downscaled results from d03, and by averaging over selected of non-TC heavy rainfall cases identified in the GFDL-ESM2M simulations. See text for details. Units of CAPE and CIN: J kg^{-1}.

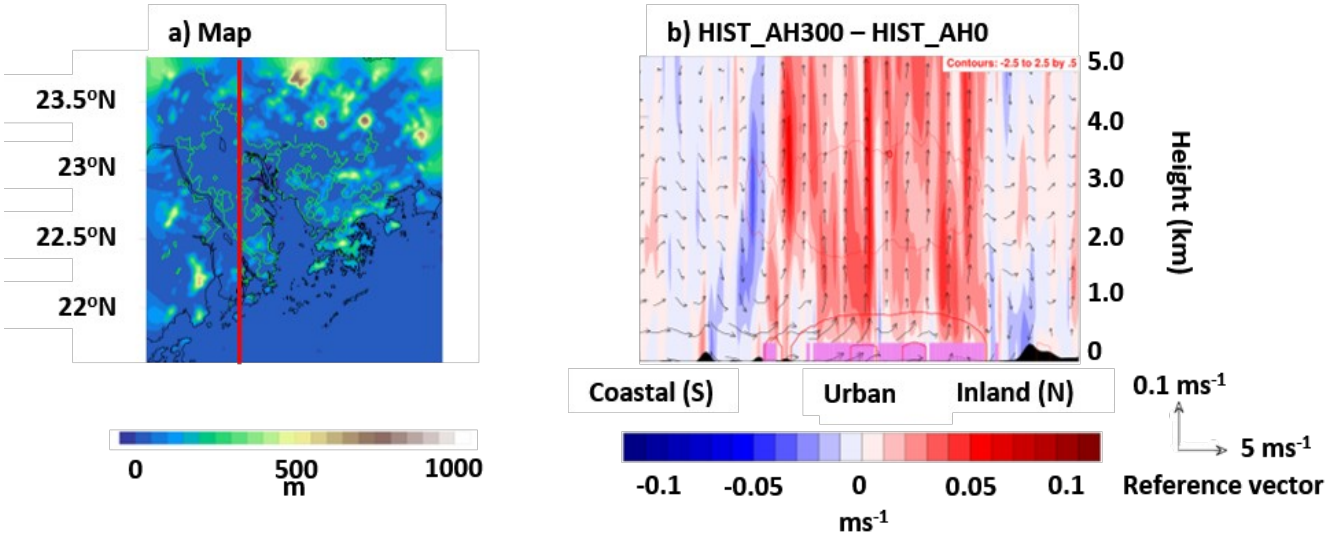

Figure 9 Vertical cross section plot of wind circulation (vectors) and vertical wind speed (shaded) anomaly of downscaled non-TC extreme cases with prevailing wind direction in N – S. (a) labelled the cross-section line, (b) is the anomaly plot of AH effect at GFDL-ESM2M historical run (HIST_300 – HIST_0). Urban locations along the cross section are indicated by pink bars in (b).

References:

Allen, L., Lindberg, F., and Grimmond, C. (2010), Global to city scale urban anthropogenic heat flux: model and variability, *International Journal of Climatology,* 31(13), 1990-2005, doi: 10.1002/joc.2210

Bell, G., (1969), The monsoon trough near the South China Coast, *Proceedings of the Conference on the Summer Monsoon of Southeast Asia*, 83-105, April 1969, https://www.hko.gov.hk/publica/reprint/r043.pdf

Bornstein, R. D. (1968), Observations of the Urban Heat Island Effect in New York City. *Journal of Applied Meteorology*, *7*, 575-582, doi:/10.1175/1520-0450(1968)007<0575:OOTUHI>2.0.CO;2.

Bornstein, R., and Lin, Q. (2000), Urban heat islands and summertime convective thunderstorms in Atlanta: three case studies, *Atmospheric Environment*, *34*(3), 507-516, doi:10.1016/S1352-2310(99)00374-X.

Bougeault, P., and Lacarrere, P. (1989), Parameterization of Orography-Induced Turbulence in a Mesobeta-Scale Model, *Monthly Weather Review*, *117*, 1872-1890 doi:10.1175/1520-0493(1989)117<1872:POOITI>2.0.CO;2.

Carlson, T. N., Dodd, J. K., Benjamin, S. G., and Cooper, J. N. (1981), Satellite Estimation of the Surface Energy Balance, Moisture Availability and Thermal Inertia, *Journal of Applied Meteorology, 20*, 67-87 doi:/10.1175/1520-0450(1981)020<0067:SEOTSE>2.0.CO;2.

Chan, L. Y., and Kwok, W. S. (2000), Vertical dispersion of suspended particulates in urban area of Hong Kong, *Atmospheric Environment*, *34*(26), 4403–4412, doi:10.1016/S1352-2310(00)00181-3.

Chan H. S., M. H. Kok, and T. C. Lee, (2012), Temperature trends in Hong Kong from a seasonal perspective, *Climate Research, 55, 53-63,* doi: 10.3354/cr01133

Changnon, S. A., and Karl, T. R. (2003), Temporal and Spatial Variations of Freezing Rain in the Contiguous United States: 1948–2000, *Journal of Applied Meteorology*, *42*(9), 1302–1315, doi:10.1175/1520-0450(2003)042<1302:TASVOF>2.0.CO;2.

Ching, J., Mills, G., el al., WUDAPT: An Urban Weather, Climate, and Environmental Modeling Infrastructure for the Anthropocene: WUDAPT is an international community-generated urban canopy information and modeling infrastructure to facilitate urban-focused climate, weather, air quality, and energy-use modeling application studies. Bulletin of the American Meteorological Society, 99(9), 1907-1924 (2018).

Chou, C., Chen, C. A., Tan, P. H., and Chen, K. T. (2012), Mechanisms for global warming impacts on precipitation frequency and intensity, *Journal of Climate*, *25*(9), 3291–3306, doi:10.1175/JCLI-D-11-00239.1.

Coceal, O., and Belcher, S. E. (2004), A canopy model of mean winds through urban areas, *Quarterly Journal of the Royal Meteorological Society*, *130*(599 PART B), 1349–1372, doi:10.1256/qj.03.40.

Collier, C. G. (2006), The impact of urban areas on weather, *Quarterly Journal of the Royal Meteorological Society*, doi:10.1256/qj.05.199.

Dee, D. P., Uppala, S. M., Simmons, A. J., Berrisford, P., Poli, P., Kobayashi, S., et al. (2011), The ERA-Interim reanalysis: Configuration and performance of the data assimilation system, *Quarterly Journal of the Royal Meteorological Society*, *137*(656), 553–597, doi: 10.1002/qj.828.

Du, S., Shi, P., and Van Rompaey, A. (2013), The Relationship between Urban Sprawl and Farmland Displacement in the Pearl River Delta, China, *Land*, *3*(1), 34–51, doi:10.3390/land3010034.

Dudhia, J. (1989), Numerical Study of Convection Observed during the Winter Monsoon Experiment Using a Mesoscale Two-Dimensional Model, *Journal of the Atmospheric*

Sciences, 46(20), doi:10.1175/1520-0469(1989)046<3077:NSOCOD>2.0.CO;2.

Dunne, J. P., John, J. G., Adcroft, A. J., Griffies, S. M., Hallberg, R. W., Shevliakova, E., et al. (2012), GFDL's ESM2 global coupled climate-carbon earth system models. Part I: Carbon system formulation and baseline simulation characteristics, *Journal of Climate*, *25*(19), 6646–6665, doi:10.1175/jcli-d-11-00560.1.

Dunne, J. P., John, J. G., Shevliakova, S., Stouffer, R. J., Krasting, J. P., Malyshev, S. L., et al. (2013), GFDL's ESM2 global coupled climate-carbon earth system models. Part II: Carbon system formulation and baseline simulation characteristics, *Journal of Climate, 26*(7), doi:10.1175/JCLI-D-12-00150.1.

Flanner, M. (2009), Integrating anthropogenic heat flux with global climate models, *Geophysical Research Letters*, 36(2), L02801, doi: 10.1029/2008gl03646

Fung, K. Y., (2018), Comparing the Urban Heat and Global Warming Impacts on Extreme Rainfall Characteristics in Pearl River Delta Based on Dynamical Downscaling, [Unpublished master's thesis]. The Chinese University of Hong Kong.

Georgescu, M., Broadbent, A., Wang, M., Krayenhoff, E. and Moustaoui, M., 2021. Precipitation response to climate change and urban development over the continental United States. Environmental Research Letters, 16(4), p.044001, doi: 10.1088/1748-9326/abd8ac

Han, J., Baik, J., and Lee, H. (2014), Urban impacts on precipitation, *Asia-Pacific Journal of Atmospheric Sciences*, 50(1), 17-30, doi: 10.1007/s13143-014-0016-7

Hartmann, D. L., Klein Tank, A. M. G., Rusticucci, M., Alexander, L. V., Brönnimann, S., Charabi, Y., Dentener, F. J., Dlugokencky, E. J., Easterling, D. R., Kaplan, A., Soden, B. J., Thorne, P. W., Wild, M., and Zhai, P. M., (2013), Observations: Atmosphere and Surface. In: *Climate Change 2013: The Physical Science Basis. Contribution of Working Group I to the Fifth Assessment Report of the Intergovernmental Panel on Climate*

Change [Stocker, T.F., Qin, D., Plattner, G.-K., Tignor, M., Allen, S. K., Boschung, J., Nauels, A., Xia, Y., Bex, V. and Midgley, P.M. (eds.)]. Cambridge University Press, Cambridge, United Kingdom and New York, NY, USA.

Heywood, G. S. P. (1953), Surface pressure-patterns and weather around the year in Hong Kong, *Technical Memoirs No. 6*, Hong Kong.

Holst, C. C., Tam, C.-Y., and Chan, J.C.L. (2016), Sensitivity of urban rainfall to anthropogenic heat flux: A numerical experiment, *Geophysical Research Letters*, *43*(5), 2240–2248.

Holst, C. C., Chan, J.C.L. and Tam, C.-Y. (2017), Sensitivity of Precipitation Statistics to Urban Growth in a Subtropical Coastal Megacity Cluster. *J. Env. Sciences,* 59, 30-38.

Hong, S.-Y., and Lim, J.-O. J. (2006), The WRF single-moment 6-class microphysics scheme (WSM6), *Journal of the Korean Meteorological Society*, *42*(2), 129–151.

Hu, C., K.W, Fung, C.-Y. Tam, and Z. Wang (2021), Urbanization impacts on Pearl River Delta extreme rainfall – sensitivity to land cover change vs anthropogenic heat, *Earth and Space Science,* DOI: 10.1029/2020EA001536

Huff, F. A., and Changnon, S. A. (1973), Precipitation modification by major urban areas, *Bulletin of the American Meteorological Society*, *54*(12), 1220–1232.

Huffman, G. J., Stocker, D. T., Bolvin, E. J., Nelkin (2014), TRMM 3B42 Precipitation Data Set. NASA Goddard Space Flight Center, doi:10.5067/TRMM/TMPA/3H/7

Iacono, M. J., Delamere, J. S., Mlawer, E. J., Shephard, M. W., Clough, S. A., and Collins, W. D. (2008), Radiative forcing by long-lived greenhouse gases: Calculations with the AER radiative transfer models, *Journal of Geophysical Research Atmospheres, 113*, doi:10.1029/2008JD009944.

Ichinose, T., Shimodozono, K., and Hanaki, K. (1999), Impact of anthropogenic heat on urban climate in Tokyo, *Atmospheric Environment*, 33(24-25), 3897-3909, doi: 10.1016/

s1352-2310(99)00132-6

Janjić, Z. I. (1994), The Step-Mountain Eta Coordinate Model: Further Developments of the Convection, Viscous Sublayer, and Turbulence Closure Schemes, *Monthly Weather Review, 122*(5), doi:10.1175/1520-0493(1994)122<0927:TSMECM>2.0.CO;2.

Kusaka, H., and Kimura, F. (2004), Thermal Effects of Urban Canyon Structure on the Nocturnal Heat Island: Numerical Experiment Using a Mesoscale Model Coupled with an Urban Canopy Model, *Journal of Applied Meteorology*, *43*(12), 1899–1910, doi:10.1175/JAM2169.1.

Kusaka, H., Kondo, H., Kikegawa, Y., and Kimura, F. (2001), A simple single-layer urban canopy model for atmospheric models: Comparison with multi-layer and slab models, *Boundary-Layer Meteorology, 101*, doi:10.1023/A:1019207923078.

Lee, T.C., K.Y. Chan, H.S. Chan and M.H. Kok, (2011), Projection of extreme rainfall in Hong Kong in the 21st century, *Acta Meteorologica Sinica, 25(6), 691–709,* doi: 10.1007/s13351-011-0601-y

Lee, T.C., H.S. Chan, E.W.L. Ginn, and M.C. Wong, (2011), Long-term trends in extreme temperatures in Hong Kong and southern China, *Adv. Atmos. Sci., 28(1), 147-157*, doi: 10.1007/s00376-010-9160-x.

Lenderink, G., Mok, H. Y., Lee, T. C., and van Oldenborgh, G. J. (2011), Scaling and trends of hourly precipitation extremes in two different climate zones - Hong Kong and the Netherlands, *Hydrology and Earth System Sciences*, *15*(9), 3033–3041, doi:10.5194/hess-15-3033-2011.

Liang, P., and Ding, Y. (2017), The long-term variation of extreme heavy precipitation and its link to urbanization effects in Shanghai during 1916–2014, *Advances In Atmospheric Sciences*, 34(3), 321-334, doi: 10.1007/s00376-016-6120-0

Liu, J., and Niyogi, D. (2019), Meta-analysis of urbanization impact on rainfall modification,

Scientific Reports, 9(1). doi: 10.1038/s41598-019-42494-2

Lo, J. C. F., Yang, Z. L., and Pielke, R. A. (2008), Assessment of three dynamical climate downscaling methods using the Weather Research and Forecasting (WRF) model, *Journal of Geophysical Research Atmospheres*, *113*(9), doi:10.1029/2007JDO09216.

Luo, Y., Zhang, R., Wan, Q., Wang, B., Wong, W., and Hu, Z. et al. (2017), The Southern China Monsoon Rainfall Experiment (SCMREX), *Bulletin of The American Meteorological Society*, 98(5), 999-1013, doi: 10.1175/bams-d-15-00235.1

McSweeney, C. F., Jones, R. G., Lee, R. W., and Rowell, D. P. (2015), Selecting CMIP5 GCMs for downscaling over multiple regions, *Climate Dynamics*, *44*(11–12), 3237–3260, doi:10.1007/s00382-014-2418-8.

Monin, A. S., and Obukhov, A. M. (1954), Basic laws of turbulent mixing in the surface layer of the atmosphere, *Inst. Contract Number*, *24*(19604), 163–187.

Nielsen, L. B., Prahm, L. P., Berkowicz, R., and Conradsen, K. (1981), Net incoming radiation estimated from hourly global radiation and/or cloud observations, *Journal of Climatology*, *1*(3), 255–272, doi:10.1002/joc.3370010305.

Oke, T. R. (1981), Canyon geometry and the nocturnal urban heat island: coparison of scale model and field observations, *J. Climatology*, *1*, 237–254.

Oke, T. R. (1988), The urban energy balance, *Progress in Physical Geography*, *12*(4), 471–508, doi:10.1177/030913338801200401.

Pan, H. L., and Wu, W.-S. (1995), Implementing a mass flux convection parameterization package for the NMC medium-range forecast model, NMC office Note No. 409. U.S. National Center for Environmental Prediction, Washington, DC.

Qian, W., Fu, J., and Yan, Z. (2007), Decrease of light rain events in summer associated with a warming environment in China during 1961-2005, *Geophysical Research Letters*, *34*(11), 1–5. doi:10.1029/2007GL029631.

Rozoff, C. M., Cotton, W. R., and Adegoke, J. O. (2003), Simulation of St. Louis, Missouri, Land Use Impacts on Thunderstorms, *Journal of Applied Meteorology and Climatology*, *42*(6), 716–738, doi:10.1175/1520-0450(2003)042<0716:SOSLML>2.0.CO;2.

Sailor, D. (2011), A review of methods for estimating anthropogenic heat and moisture emissions in the urban environment, *International Journal of Climatology*, 31(2), 189-199, doi: 10.1002/joc.2106

Shepherd, J. M. (2005), A review of current investigations of urban-induced rainfall and recommendations for the future, *Earth Interactions*, *9*(12), doi:10.1175/EI156.1.

Sisterson, D. L., and Dirks, R. A. (2015), The urban moisture climate, *Proceedings of the Conference on Metropolitan Physical Environment.*, *Gen. Tech.*, 26–35.

Skamarock, W. C., Klemp, J. B., Dudhi, J., Gill, D. O., Barker, D. M., Duda, M. G., et al. (2008), A Description of the Advanced Research WRF Version 3, *Technical Report*, (June), 113, doi:10.5065/D6DZ069T.

Smirnov, N. (1948). Table for Estimating the Goodness of Fit of Empirical Distributions. The Annals Of Mathematical Statistics, 19(2), 279-281. doi: 10.1214/aoms/1177730256

Tewari, M., F. Chen, W. Wang, J. Dudhia, M. A. LeMone, K. Mitchell, M. Ek, G. Gayno, J. Wegiel, and R. H. Cuenca (2004), Implementation and verification of the unified NOAH land surface model in the WRF model, *20th conference on weather analysis and forecasting/16th conference on numerical weather prediction*, 11–15.

Ueda, H., Iwai, A., Kuwako, K., and Hori, M. E. (2006), Impact of anthropogenic forcing on the Asian summer monsoon as simulated by eight GCMs, *Geophysical Research Letters*, *33*(6), 20–23, doi:10.1029/2005GL025336.

Wai, M. K., Welsh, T., and Ma, W. M. (1995), The Timing and Distribution of Summer Convective Rainfall Over Hong Kong and South China, *Hong Kong Meteorological Society Bulletin*, 5(2), https://www.hko.gov.hk/publica/reprint/r300.pdf

Wang, R., Cai, M., Ren, C., Bechtel, B., Xu, Y., and Ng, E., Detecting multi-temporal land cover change and land surface temperature in Pearl River Delta by adopting local climate zone. Urban Climate, 28, 100455 (2019).

Wilby, R. L., Troni, J., Tedd, L., Hewitson, B. C., Smith, D. M., and Sutton, R. T. (2009), A review of climate risk information for adaptation and development planning, *International Journal of Climatology*, *29*(9), 1193–1215.

Wong, M., Mok, H., and Lee, T. (2010), Observed changes in extreme weather indices in Hong Kong, *International Journal of Climatology*, 31(15), 2300-2311, doi: 10.1002/joc.2238

Wong, M. S., Yang, J., Nichol, J., Weng, Q., Menenti, M., and Chan, P. W. (2015), Modeling of Anthropogenic Heat Flux Using HJ-1B Chinese Small Satellite Image: A Study of Heterogeneous Urbanized Areas in Hong Kong, *IEEE Geoscience and Remote Sensing Letters, 12*, 1466-1470, doi:10.1109/LGRS.2015.2409111.

Zhang, Q., Xu, C., Becker, S., Zhang, Z., Chen, Y., and Coulibaly, M. (2009), Trends and abrupt changes of precipitation maxima in the Pearl River basin, China, *Atmospheric Science Letters*, 10(2), 132-144, doi: 10.1002/asl.221

Zhang, H., Wu, C., Chen, W., and Huang, G. (2019), Effect of urban expansion on summer rainfall in the Pearl River Delta, South China, *Journal of Hydrology*, 568, 747-757, doi: 10.1016/j.jhydrol.2018.11.036